

Origins of Very Low Helium Abundance Streams Detected in the Solar Wind Plasma

YOGESH ^{1,2,3} N. GOPALSWAMY,² D. CHAKRABARTY,⁴ PARISA MOSTAFAVI,⁵ SEIJI YASHIRO,^{2,3} NANDITA SRIVASTAVA,⁶ AND
LEON OFMAN ^{2,3,7}

¹previously at Physical Research Laboratory, Navrangpura, Ahmedabad 380009, India

²NASA Goddard Space Flight Center, Greenbelt, MD, 20771, USA

³The Catholic University of America, Washington, DC 20064, USA

⁴Physical Research Laboratory, Navrangpura, Ahmedabad 380009, India

⁵Johns Hopkins University, Applied Physics Lab. Laurel, MD 20723, USA

⁶Udaipur Solar Observatory, Physical Research Laboratory, Udaipur, 313001, India

⁷Visiting, Tel Aviv University, Tel Aviv, Israel

ABSTRACT

The abundance of helium (A_{He}) in the solar wind exhibits variations typically in the range from 2-5% with respect to solar cycle activity and solar wind velocity. However, there are instances where the observed A_{He} is exceptionally low ($< 1\%$). These low- A_{He} occurrences are detected both near the Sun and at 1 AU. The low A_{He} events are generally observed near the heliospheric current sheet. We analyzed 28 low- A_{He} events observed by the *Wind* spacecraft and 4 by Parker Solar Probe (PSP) to understand their origin. In this work, we make use of the ADAPT-WSA model to derive the sources of our events at the base of the solar corona. The modeling suggests that the low- A_{He} events originated from the boundaries of coronal holes, primarily from large quiescent helmet streamers. We argue that the cusp above the core of the streamer can produce such very low helium abundance events. The streamer core serves as an ideal location for gravitational settling to occur as demonstrated by previous models, leading to the release of this plasma through reconnection near the cusp, resulting in low A_{He} events. Furthermore, observations from Ulysses provide direct evidence that these events originated from coronal streamers.

Keywords: Solar wind — Sun: abundances — Sun: heliosphere — Sun: corona — Sun: magnetic fields

1. INTRODUCTION

Helium abundance (A_{He}) in the solar wind relative to protons is defined as $A_{He}=100\times N_a/N_p$, where N_a and N_p are the number densities of alpha particles (referred interchangeably as ‘helium’ in this paper, since He^{++} is the dominant helium ion in the corona and in the solar wind) and protons. A_{He} is known to vary significantly throughout the solar atmosphere (Moses et al. 2020). Depending on the sources, coronal, and interplanetary modulations, A_{He} can range from 0.1% to more than 30% in number density ratio. If we consider the mass of He, it can account for the bulk of the solar wind mass flux at the high end of the abundance. A_{He} follows the solar cycle (SC) and varies with solar wind velocity (Kasper et al. 2007; Alterman & Kasper 2019; Yogesh et al. 2021; Alterman et al. 2021). It has been shown that A_{He} is 8% in the photosphere and decreases to 4-5% in the solar corona. It can increase up to 30% in coronal mass ejections (Yogesh et al. 2022, and references therein). The enhancement of elemental abundances with low First Ionization Potential (FIP) in chromosphere, transition region, and coronal loops is known as the FIP effect. The FIP effect can also affect the relative abundances of heavy ions in the various coronal regions at the sources of the solar wind (see the review by Laming 2015). The FIP effect can enhance low ($<10\text{eV}$) FIP elements (e.g., Mg, Fe etc.) and reduce high FIP ($>10\text{eV}$) elements (e.g. He, Ne etc.) in the corona (Laming et al. 2019). The variation of the helium abundance relative to protons in coronal streamers was modeled with 2.5D three-fluid models, demonstrating the gravitational settling in the core of streamers and their expected observational signatures (Ofman 2004a; Giordano et al. 2007; Ofman & Kramar 2010; Abbo et al. 2016; Ofman et al. 2024). The helium abundance also varies in the interplanetary (IP) medium depending on the interaction between different solar wind streams (Đurovcová et al.

2019; Yogesh et al. 2023). Interactions between the helium ions and protons in the fast wind stream produced by Alfvén waves in coronal holes were modelled (Ofman 2004b). The signatures of the periodic reconnections of the flux tubes carrying Alfvén waves are also found in the abundances at 1AU (Gershkovich et al. 2023; Kepko et al. 2024). The variation in the helium abundance can tell us about the different processes occurring near the solar surface and interplanetary medium and the sources of the solar wind. The variation of A_{He} in the solar wind (Kasper et al. 2007; Alterman & Kasper 2019; Yogesh et al. 2021), CMEs (Fu et al. 2018; Yogesh et al. 2022), SIRs (Yogesh et al. 2023, and references therein), has been explored by various researchers. However, there are very few works on the very low ($< 1\%$) helium abundances in the solar wind. This is a significant problem as understanding very low helium abundances may provide important insights on the generation and propagation of the solar wind.

Borrini et al. (1981) demonstrated on the basis of observations of IMP 6, 7, and 8 that the helium abundance is low near sector boundaries in the interplanetary (IP) medium. They also showed that these regions are generally associated with higher proton and electron densities, IP field polarity reversals, low bulk velocity, low alpha (T_a) and proton (T_p) temperature, minimum in the T_a/T_p ratio and nearly equal proton and alpha speed. They suggested that these events may be related to the streamer belts and might be associated with the solar current sheets. However, the processes that could decrease A_{He} so drastically were not addressed. Also, it remains unclear whether these reductions in the A_{He} are because of the interplanetary modulations or due to processes closer to the Sun.

Recently, a few other researchers (e.g., Sanchez-Diaz et al. 2016; Vasquez et al. 2017) studied the low helium abundances using Helios spacecraft observations. A low helium abundance was detected in the very slow solar winds (VSSW, velocity $< 300\text{km/s}$) (Sanchez-Diaz et al. 2016). They showed that A_{He} in VSSW varies with the SC and the velocity of helium ions was less than that of protons in VSSW events. During solar maxima, A_{He} value in the VSSW was higher than that in the normal slow wind (velocity $> 300\text{km/s}$) in a few events. Although the main objective of these authors was to understand the properties of VSSW, they showed that these events were related to the Heliospheric Current Sheets (HCS) and High-Density Regions (HDR). Vasquez et al. (2017) studied A_{He} in very slow ejecta and winds near the solar minima of SC23. They found that slow ejecta and winds show similar A_{He} variation. Additionally, they observed that these events conform to the relationship between A_{He} and solar wind velocity previously established by Kasper et al. (2007). However, this relationship was not followed at a very low solar wind speed. The physical reason behind the low A_{He} events and their sources have not been explored in depth so far.

Woolley et al. (2021) and Ofman et al. (2023) reported very low helium abundance ($< 1\%$) observed by Parker Solar Probe (PSP) at perihelia. Based on data from the Ulysses and ACE spacecraft, Suess et al. (2009) found a significant reduction in helium abundance near quiescent current sheets. They suggested that the low A_{He} events are generally observed near the HCS and streamers. The observation of low A_{He} has been reported in the past by various researchers, but the process causing this depletion is unclear to a large extent. To address this gap, we critically examined the solar sources of these events. We have used the data from PSP, *Wind*, ACE, and Ulysses to show that these events are observed through the heliosphere and originate from similar sources. We also make use of the Wang-Sheeley-Argge (WSA) model (Arge & Pizzo 2000; Arge et al. 2003b, 2004; McGregor et al. 2008) driven by Air Force Data Assimilative Photospheric Flux Transport (ADAPT: Arge et al. 2009, 2010, 2013; Hickmann et al. 2015) time-dependent photospheric field maps to derive the coronal magnetic field, as well as source regions of these events at $1 R_{\odot}$. The data used and model details are presented in Section 2. Section 3 shows the results. The likely reasons behind the reduction in A_{He} are discussed in Section 4.

2. DATA SELECTION AND MODEL DETAILS

We selected 28 events for which very low A_{He} ($< 1\%$) condition persists for more than 48 hours at the Sun-Earth L1 point using hourly averaged data from the Solar Wind Experiment (SWE, Ogilvie et al. 1995) onboard the *Wind* spacecraft. Hourly averaged data removes the problems associated with transient spikes and data gaps in A_{He} . If we consider the full-cadence (92 seconds) data, A_{He} remains below 1% except for a few spikes. The data from SWE (Ogilvie et al. 1995) and Magnetic Field Investigations (MFI) (Lepping et al. 1995) instruments on board the *Wind* satellite are used for proton, alpha parameters, and magnetic field, respectively. To identify the events, we used SWE data quality flag greater than 1, as our focus was on the alpha and proton densities. We find that most of the events are during the solar minima period, i.e. 1995-1996, 2007-2010, 2017-2021. The list of the selected events can be found in supplementary table S1.

To analyze the low A_{He} (four) events close to the Sun, we used data from the Solar Probe Analyzer for Ions (SPAN-I), which is a subsystem of the Solar Wind Electrons Alphas and Protons (SWEAP) (Kasper et al. 2016) onboard

PSP. SPAN-I has a Time-of-Flight section for mass-per-charge determination and can provide the alpha and proton parameters (Livi et al. 2022). The magnetic field observations are used from the FIELDS instrument suite (Bale et al. 2016). In this paper, we focused on times when the PSP made its closest approaches (i.e., ‘encounters’), ensuring that the spacecraft’s tangential velocity was enough for SPAN-I to observe the core of the protons and alpha particle distributions. More details regarding the selection of appropriate data from SPAN-I can be found in Mostafavi et al. (2022). We did not map the events between PSP and *Wind*.

In this work, we use *Wind* data to study the variation in solar wind parameters because of the availability of high cadence data. We also use the Advance Composition Explorer (ACE; Stone et al. 1998) data to compare the ADAPT-WSA model output and interplanetary data. The *Wind* and ACE observations have a high correlation in the case of most of the events. ACE’s Solar Wind Ion Composition Spectrometer (SWICS; Gloeckler et al. 1998) data are used to quantify compositional (Fe/O) changes during the events. We utilized SWICS 1.1 and SWICS 2.0 data (two-hour cadence) combined to span from 1998 to 2020. Data from the SWOOPS payload (Bame et al. 1992) onboard Ulysses spacecraft are also used to provide the heliolatitude variation of helium abundance.

We have used the ADAPT-WSA model to derive the coronal magnetic field and source region at $1 R_{\odot}$ for all the events. WSA is an empirical and physics-based model that derives the coronal field using a coupled set of potential field type models. The first is a traditional magnetostatic potential field source surface (PFSS) model (Schatten et al. 1969; Altschuler & Newkirk 1969; Wang & Sheeley 1992), which determines the coronal field out to the source surface height. For this event, the traditional height of $2.5 R_{\odot}$ (Hoeksema et al. 1983) is used. The PFSS solution then serves as input into the Schatten Current Sheet (SCS) model (Schatten 1971), which provides a more realistic magnetic field topology of the upper corona (e.g. from $2.5-21.5 R_{\odot}$). An empirical velocity relationship (Arge et al. 2003a, 2004; Wallace et al. 2020) is then used to derive the solar wind speed at the outer coronal boundary, that is a function of both magnetic expansion factor as defined in Wang & Sheeley (1990) and the minimum angular separation between a field line foot point and the nearest coronal hole boundary (e.g., coronal hole boundary distance, as defined in Riley et al. 2001, 2015). The model then propagates solar wind parcels outward from the endpoints of each magnetic field line connected to the spacecraft while incorporating a simple 1-D modified kinematic model, which accounts for stream interactions by preventing fast streams from bypassing slow ones (Arge et al. 2004). The model determines the time of arrival of these solar wind parcels at *Wind*/ACE and PSP, allowing us to connect the in situ observed solar wind back to their model-determined solar origin.

Synchronic photospheric field maps used as input to the WSA model were generated using the ADAPT model driven by Global Oscillations Network Group (GONG) magnetograms. ADAPT utilizes flux transport modelling (Worden & Harvey 2000), to account for solar time-dependent phenomena (e.g. differential rotation, meridional and supergranulation flows) for locations on the Sun in which photospheric field measurements are not available (e.g. *poles and far-side*). The best model output is determined by comparing the model-derived and observed radial magnetic field and solar wind speed.

3. RESULTS

3.1. *In-situ measurements of low helium abundance events*

The low helium abundance ($A_{He} < 1\%$) events are identified using *Wind* and PSP data. The events identified based on PSP data have shorter duration since the position of PSP changes rapidly at or near perihelia. PSP events are chosen based on SPAN-I data coverage, i.e., when alpha and proton measurements are both available and in the field of view of the instrument. Proper field-of-view criteria are important to avoid misinterpretation of PSP data. We found four such events from encounter 4 (2 events), 9 and 11 (see, Ofman et al. 2023, for additional $A_{He} < 1\%$ PSP events). The details regarding *Wind* and PSP events are provided in the supplementary table S1.

This section discusses the December 2019 event (number-21) observed by *Wind* (see Fig. 1). The other events are analyzed similarly, and the results are provided in the supplementary table S1. The Panels 1a-1f of Figure 1 present magnetic field components, speed (alpha and proton), number density (proton and alpha), helium abundance, the temperature of the proton (T_p) and alpha (T_a), and differential speed ($\Delta v = |v_a| - |v_p|$). It can be seen from Figure 1 that this marked event has low speed (average ~ 310 km/s). All the other events also show a similar lower speed. The blue and red horizontal dashed lines in Figure 1c show the SC average of proton and alpha number density, respectively. It is seen that the proton number density is usually higher or equal to the average value almost all the time. In contrast, the helium number density is (with a few occasional spike-like increases) significantly less than the average helium number density during the interval marked by the vertical red dashed lines. The time of vertical lines

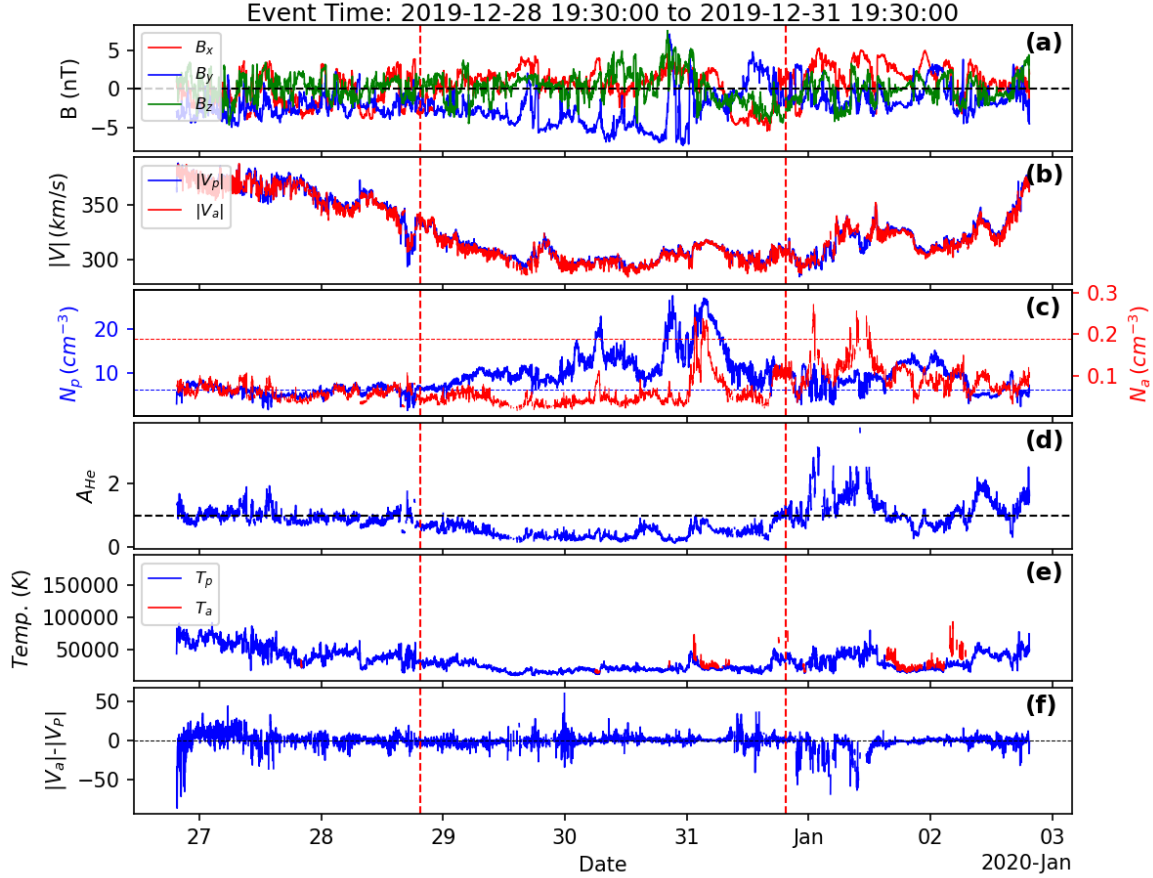


Figure 1. A low helium abundance event observed by *Wind* spacecraft in December 2019. The red vertical lines show the start and time of the event. The variations of the magnetic field components, speed (proton and alpha), number density (proton and alpha), helium abundance, proton and alpha temperature (T_p , T_a), and differential speed, are shown in panels *a* to *f*. The blue and red horizontal lines in panel *c* represent the average number density of protons and alpha particles over two solar cycles (SCs). Panel *c* shows that the proton density (N_p) is higher than the average value of N_p (6.29) over the two SCs. In panel *c*, the scale for proton density is on the left side and alpha density is on the right side. On the contrary, alpha particle densities are lower than the two solar cycle averaged values. There is significantly less speed difference between the alphas and protons (see panel *f*).

is given in the plot title. Figure 1d plots A_{He} . The black dashed line in this panel is $A_{He}=1\%$. A similar parameter variation is observed for the other 28 events as well. This suggests that the reduction in alpha number density causes these very low A_{He} events. We select intervals for which the helium abundance remains continuously below 1% for more than 48 hours.

Figure 2 shows PSP event (number 2) from January 2020 from the supplementary Table S1. The event shown here is from encounter 4 when PSP was at a distance of 0.13 AU ($27.8 R_{\odot}$). The variation of all the parameters shown in Figure 2 is in the instrument frame. This does not impact our interpretation of the data because we are primarily focusing on density. The parameter format matches Figure 1. Figure 2 (a-f) shows magnetic field components, the bulk velocity of alphas and protons, alpha and proton number density, helium abundance, T_p , T_a and difference in the bulk velocities of alphas and protons.

Figure 2 shows that the low A_{He} interval (except for occasional spikes) is not only confined to the defined interval of encounter 4 but also extended more than 12 hours before and after the interval. Unlike in Figure 1, there is a finite speed difference between the alphas and protons in the event duration. The differential speed close to the Sun is much larger than that at 1 AU. This is shown in Mostafavi et al. (2024), who compared the observations at PSP and L1 data. The differential speed between the protons and alphas decreases as they propagate, possibly because of collisions they experience during propagation, or due to kinetic instabilities and wave-particle interaction (e.g., Kasper et al. 2017;

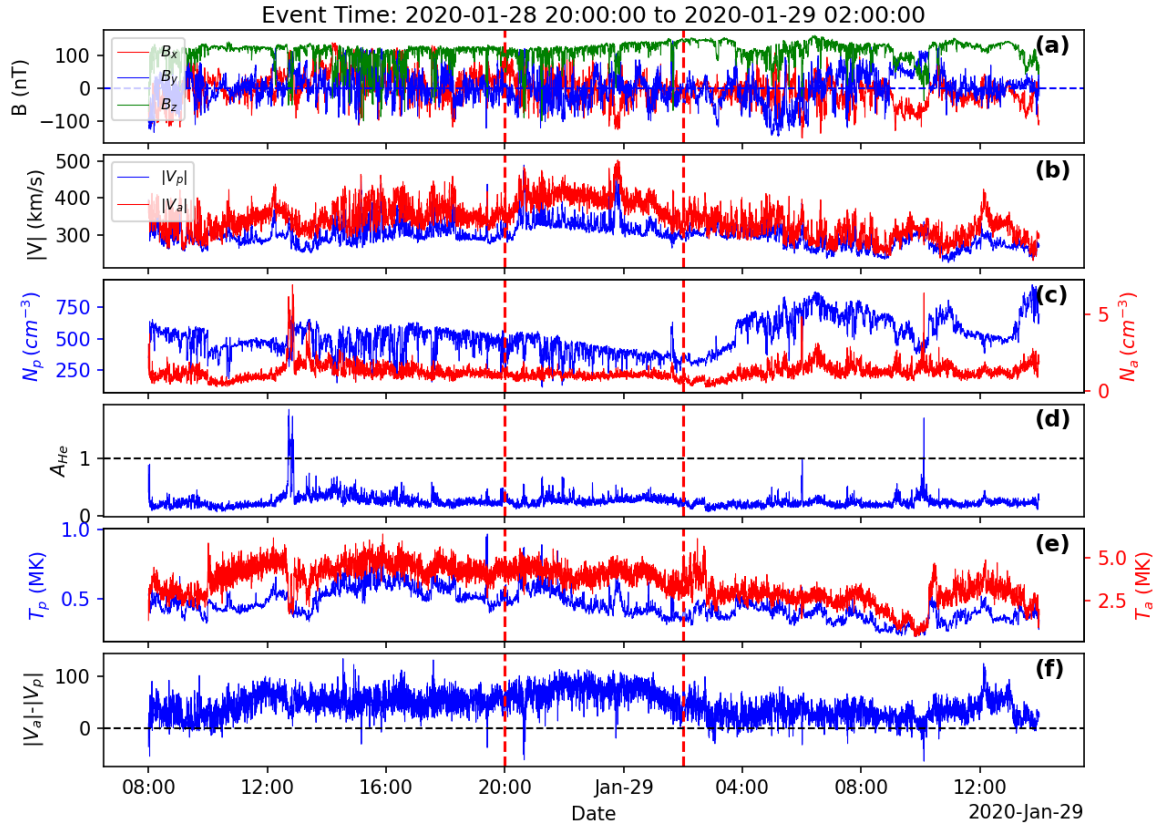


Figure 2. The low helium abundance event observed by PSP in January 2020. Similar to Figure 1, the variations in the solar wind parameters are shown in panels *a* to *f*. The event time is selected based on the presence of alpha and protons in the field of view of the SPAN-I instrument onboard PSP. The vertical lines indicate the duration of the event during which the helium and hydrogen cores were within the field of view of the SPAN-I instrument and A_{He} remained below 1%. The dashed horizontal lines in panels *a*, *d*, *f* are $B=0$, $A_{He}=1\%$ and zero differential speed, respectively.

Alterman et al. 2018; Āurovcova et al. 2019). Interestingly, this speed difference is reduced after the event, and the solar wind is also slower than average. This extended part also shows properties similar to the events observed at L1 by *Wind*. The discrepancy between T_a and T_p observations at L1 and PSP are likely due to collisions and wave-particle interaction that the ions experience as they propagate (Mostafavi et al. 2024). Although this PSP event shows much lower A_{He} as compared to *Wind* events, other PSP events demonstrate A_{He} values similar to those observed by the *Wind* spacecraft.

3.2. Back tracing of sources of low Helium abundance events

Figures 3 and 4 show the ADAPT-WSA model output of the coronal magnetic field and sources of the *Wind* and PSP events discussed in the previous section and shown in Figures 1 and 2. The top panel in Figure 3 and 4 show the WSA-derived coronal holes and the spacecraft connectivity (marked by the black lines) between the projection of *Wind*/PSP’s location at $5 R_\odot$ (red/white tickmarks) and open field foot-points at $1 R_\odot$. The black lines reveal the model-derived source regions of the solar wind observed at *Wind*/PSP. The dates in red refer to the location of each spacecraft in time over a Carrington rotation. These dates correspond to when the solar wind left the Sun as opposed to when it arrived at the spacecraft. The middle panel shows the spacecraft connectivity to the photospheric ($1 R_\odot$) magnetic field, and the bottom panel shows the coronal magnetic field at $5 R_\odot$. The color bar represents model-derived solar wind speed in the same panel. The three panels are shown for the whole Carrington rotation (Figure 3: CR 2225, Figure 4: CR 2226). Figure 3 and 4 shows that the two solar wind events discussed in the previous section that were observed on 28-31 Dec 2019 at *Wind* and 28-29 Jan 2020 at PSP which originated from a large global helmet streamer connected with the boundaries of coronal holes.

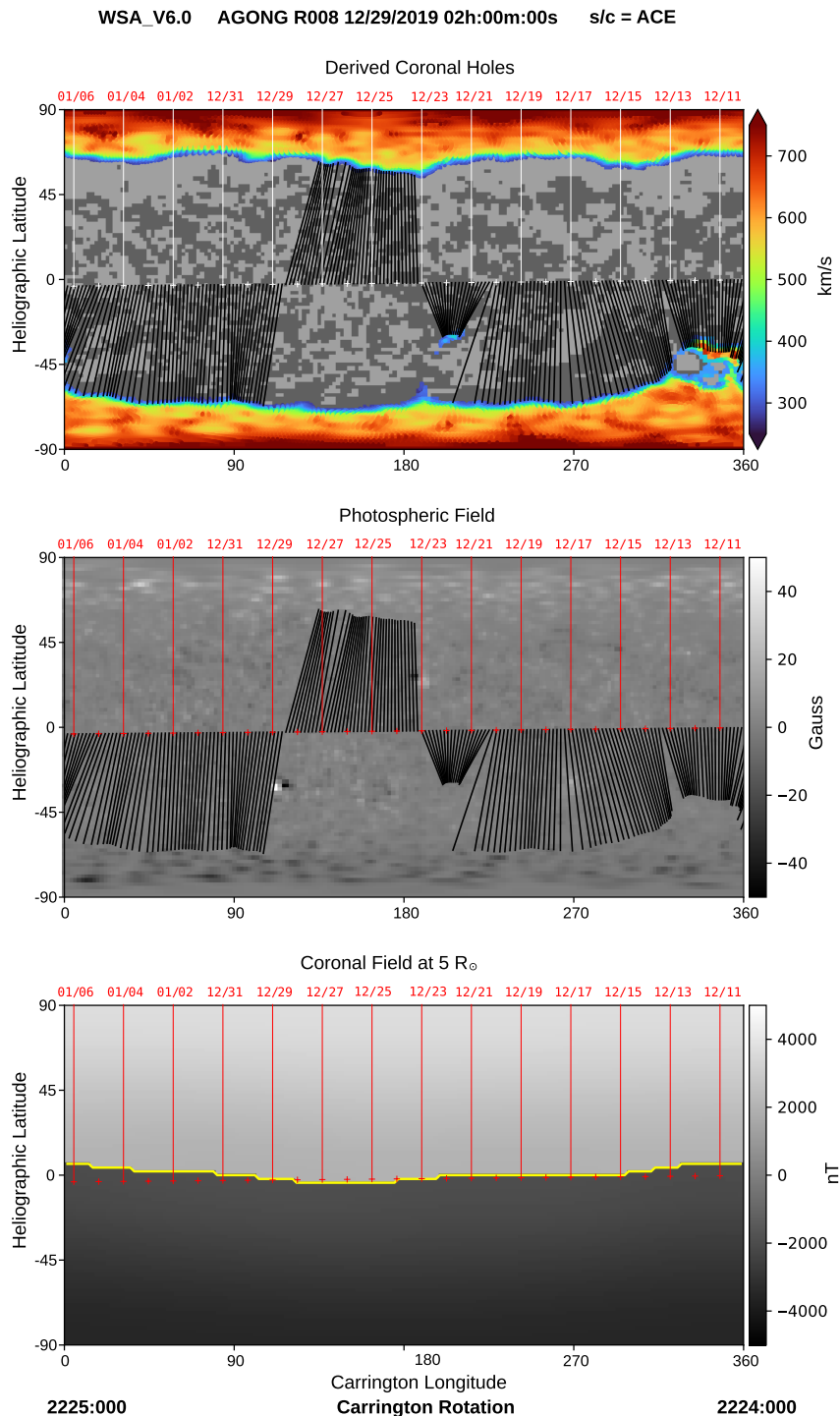


Figure 3. ADAPT-WSA model output for CR 2225. The model run is for *Wind* (or ACE) event (corresponding to Figures 1). The white (top panel) and red (middle and bottom panel) tick-marks or vertical lines represent the back projection of the *Wind* satellite at $5 R_{\odot}$. The top panel shows a WSA-derived open field at $1 R_{\odot}$ with model-derived solar wind speed in color scale. Black lines indicate the magnetic connectivity between the projection of the observing satellite location at $5 R_{\odot}$ and the solar wind source region at $1 R_{\odot}$. The field polarity at the photosphere is indicated by the light/dark (positive/negative) grey contours in the same upper panel. The photospheric field can be seen in the middle panel. This panel's black lines again show the connectivity between the ACE, and the photosphere. The bottom panel shows the WSA-derived coronal field at $5 R_{\odot}$. The yellow contour marks the model-derived heliospheric current sheet, where the overall coronal field changes sign.

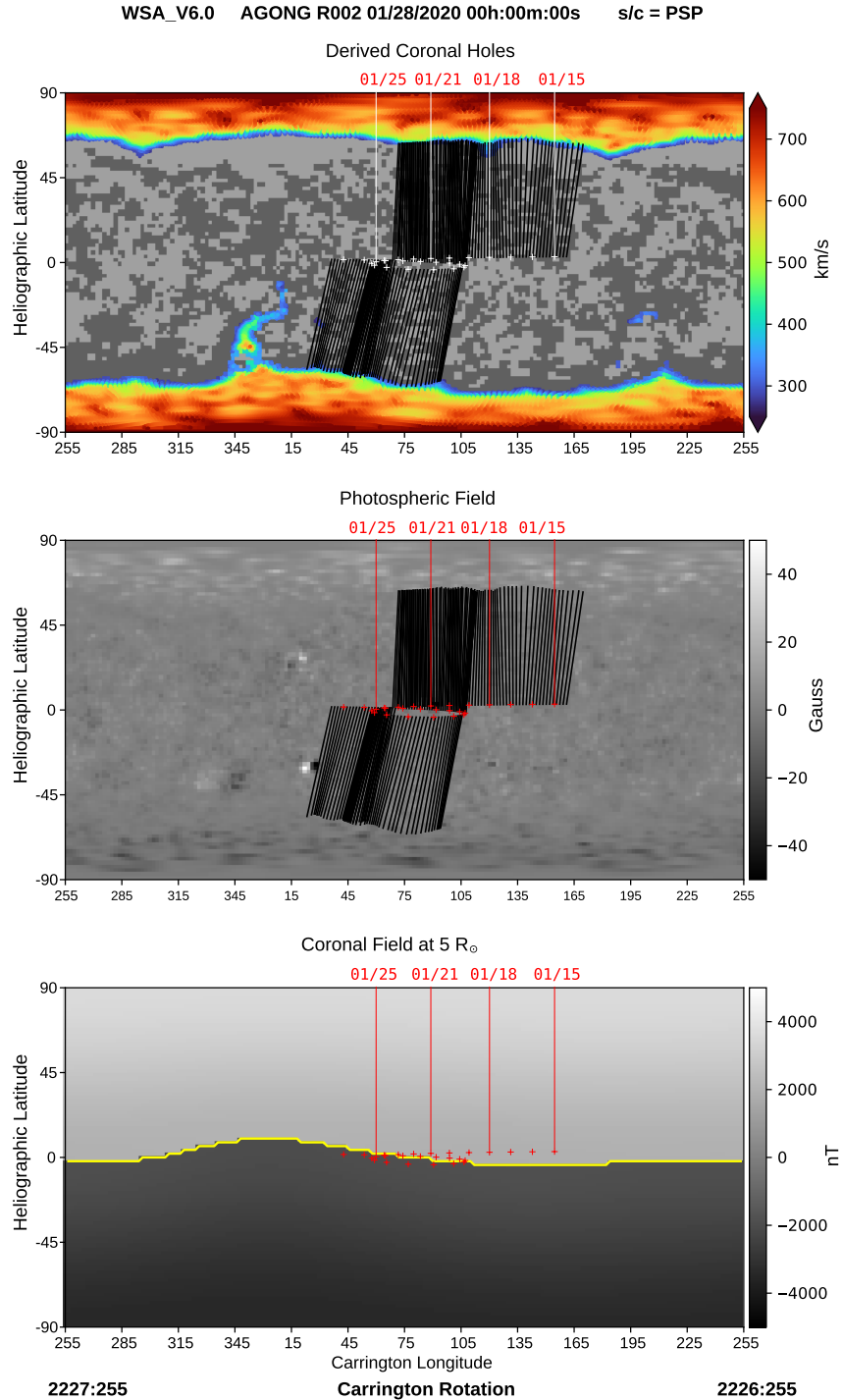


Figure 4. Similar to figure 3, ADAPT-WSA model output for CR 2226. The model run is for PSP event, respectively (corresponding to Figures 2). The white (top panel) and red (middle and bottom panel) tick-marks or vertical lines represent the back projection of the PSP satellite at $5 R_{\odot}$. The top panel shows a WSA-derived open field at $1 R_{\odot}$ with model-derived solar wind speed in color scale. Black lines indicate the magnetic connectivity between the projection of the observing satellite location at $5 R_{\odot}$ and the solar wind source region at $1 R_{\odot}$. The field polarity at the photosphere is indicated by the light/dark (positive/negative) grey contours in the same upper panel. The photospheric field can be seen in the middle panel. This panel's black lines again show the connectivity between the PSP, and the photosphere. The bottom panel shows the WSA-derived coronal field at $5 R_{\odot}$. The yellow contour marks the model-derived heliospheric current sheet, where the overall coronal field changes sign.

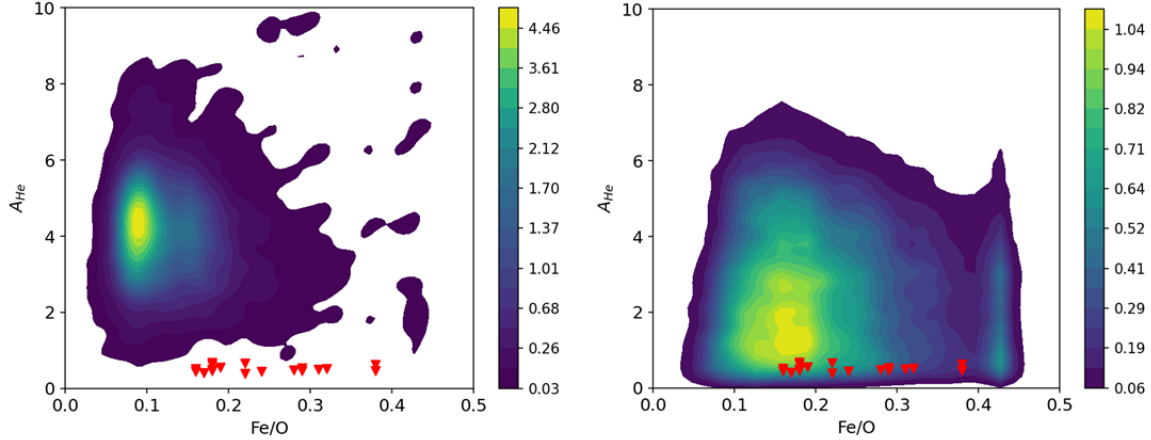


Figure 5. The Fe/O vs A_{He} density distributions from ACE SWICS data in fast wind (>600 km/s, left) and slow wind (<450 km/s, right). The red patches show our events' average A_{He} and Fe/O values.

We also use WSA model parameters derived for each of the 28 *Wind* events and 4 PSP events to further characterize the solar sources that produce low helium abundance in the solar wind and report them in Supplementary Table S2. The model parameters are calculated for the identified field lines that are the source of each event. It is important to note that the model-derived field lines identified as the sources of these events only relate to a 2D slice that the spacecraft connects to, which is a part of a much larger and complex 3D magnetic field topology. Even still, these model-determined sources help inform us about the sources of the low A_{He} events. The model calculations are best matched for the events' duration instead of an entire Carrington rotation. This comparison helps in the improved identification of sources for the specific time periods of our low A_{He} intervals.

We have verified that the sources of almost all the events are coronal hole boundaries as the average minimum angular separation between the field lines identified as the sources of these events and the nearest coronal hole boundary is less than 4° (see supplementary Table S2). These coronal hole boundaries are generally linked with large-scale quiescent streamers (Higginson et al. 2017) which suggests that these events originate from the coronal streamers. Additionally, almost all of these events occur within 10° of the heliospheric current sheet (HCS), which is formed by coronal bipolar (helmet) streamers (Wang et al. 2000). Many of these events are associated with magnetic fields that have moderate to high expansion factors, which act as proxies for solar wind speed. This suggests that the sources of these events are located at or near coronal hole boundaries. Although one might typically expect higher expansion factors at coronal hole boundaries, the expansion factor is directly dependent on the photospheric field strength at the field line footpoint. Most of these events are linked to quiet Sun magnetic fields. Interestingly, the sources of these events are independent of the observation point in the heliosphere, whether observed by PSP or *Wind*. The role of these source regions in the context of low helium abundance events is discussed in the upcoming sections.

3.3. Comparison of Fe/O and A_{He}

In the previous subsection, we found that these events originated from streamers, which can provide plasma from the coronal hole, cusp and legs (Suess et al. 2009). In order to understand the contribution of the coronal hole plasma, we compare the density distribution of Fe/O vs A_{He} for the fast-solar wind events (left panel of Figure 5) with that during the slow wind events (right panel of Figure 5). For this purpose, data from the ACE satellite from 1998 to 2020 are used. Because we select 48 hours long intervals, we consider propagation effects between ACE and *Wind* to be minimal. The right panel of Figure 5 is pertinent for the low A_{He} events. We include the fast wind in the left panel for comparison. Figure 5 indicates that the Fe/O ratio of the slow wind events are predominantly located at the higher values of Fe/O. The red patches in both the panels of Figure 5 are A_{He} and Fe/O values averaged for the entire duration of the low A_{He} events considered in the present work. Interestingly, these patches are outside the observed distribution of the fast wind but inside the distribution corresponding to the slow wind. Further, these events significantly deviate from the distribution of fast wind, suggesting a minimal contribution from coronal hole plasma. We also compared the events separately using SWICS 1.1 and SWICS 2.0. There was a shift in the absolute values, but this does not impact our inferences.

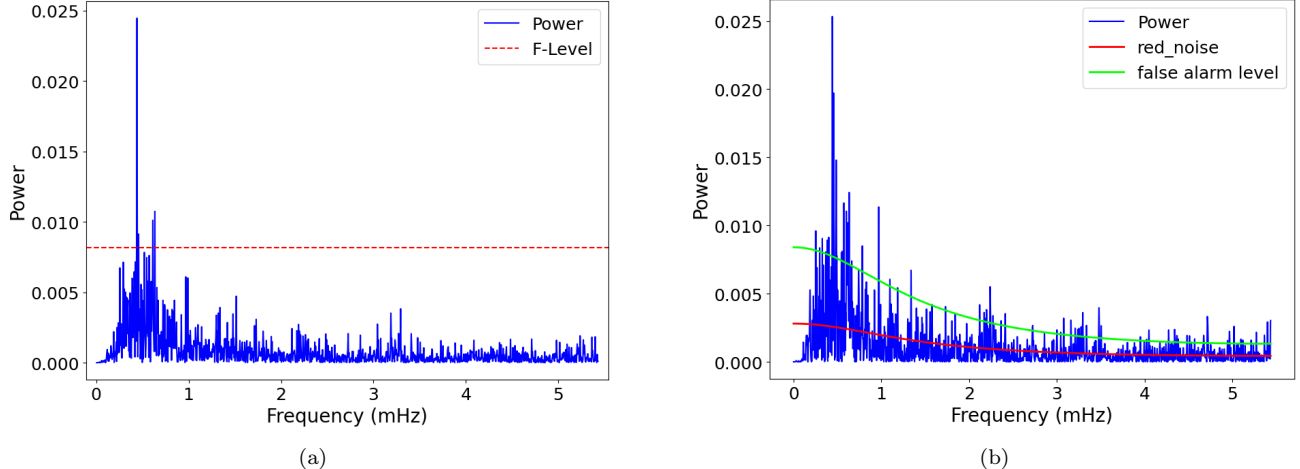


Figure 6. The FFT with Fisher’s false alarm test (F-level, left panel) and Lomb-Scargle periodogram analysis with red noise and chi-95% significance level (right panel) for the event shown in Figure 1. It can be seen in both panels that the frequency of 0.44 mHz (period 2270 sec) shows the highest power.

3.4. Signatures of the periodic reconnections

Suess et al. (2009) suggested that plasma blobs are released through the cusp of the streamers. The sharply pinched magnetic field confines the plasma, and this plasma can be released easily by small pressure pulses. In this section, we have explored the presence of these periodic pressure pulses caused by Alfvén waves. We have performed the fast Fourier transform (FFT) and the Lomb-Scargle periodogram on A_{He} time series. Figure 6 shows the frequencies present in the event (number 21) present in Figures 1.

We also conducted the Fisher test and red noise levels to check the significance of the periods during these events. Figure 6 shows the FFT with Fisher’s false alarm test (F-level, left panel) and Lomb-Scargle periodogram analysis with red noise and chi-95% significance level (right panel). The frequency of 0.44 mHz (period ~ 2270 sec) has a high power (above the false alarm and Fisher’s F-level), suggesting the presence of a clear signature of characteristic Alfvénic waves. The interchange reconnection model proposed by Lynch et al. (2014) has a characteristic timescale of approximately 2,000 seconds, corresponding to a frequency of about 0.5 mHz, which is comparable to the global Alfvén frequency. This provides indirect evidence to the proposition that episodic release of low A_{He} parcels from the streamer cusps are triggered by Alfvén waves. Periodicities around 0.44 mHz were also observed by Gershkovich et al. (2023) in various solar wind compositions. Similar analyses were performed for all *Wind* and *PSP* events, and almost all events showed similar periods (see supplementary Table S3). The top 5 significant periods are listed in the table.

3.5. Low helium abundance in *Ulysses* observations

To further characterise the origin of this class of events, we have used *Ulysses* data to examine the heliographic variations of the helium abundance. Figure 7 shows the A_{He} variation with helio-graphic latitudes. The red circle represents the $A_{He}=1\%$. The first (left panel) and third (right panel) orbit represent the solar minima, whereas the second (middle panel) one shows the solar maxima. It can be observed from Figure 7 that the $A_{He} < 1\%$ events are present near the equatorial plane during solar minima (Orbit 1 and 3), and these events are distributed towards higher heliolatitudes during the solar maxima (Orbit 2).

4. DISCUSSION

The low helium abundance events are important as they can provide critical information regarding the sources of solar wind and possibly clues on the acceleration mechanism. These events are observed throughout the heliosphere. Coronal hole boundaries are source regions for the slow solar wind (Schwadron et al. 2005; Abbo et al. 2016). The slow solar wind usually has a lower A_{He} than the fast wind and is highly variable (Kasper et al. 2007; Sanchez-Diaz et al. 2016). The analysis presented in the previous section demonstrates that the sources of very low helium events are associated with streamers. A detailed discussion regarding the association of the low A_{He} events with the streamers can also be found in Suess et al. (2009). Borrini et al. (1981) also showed that low helium abundances are observed

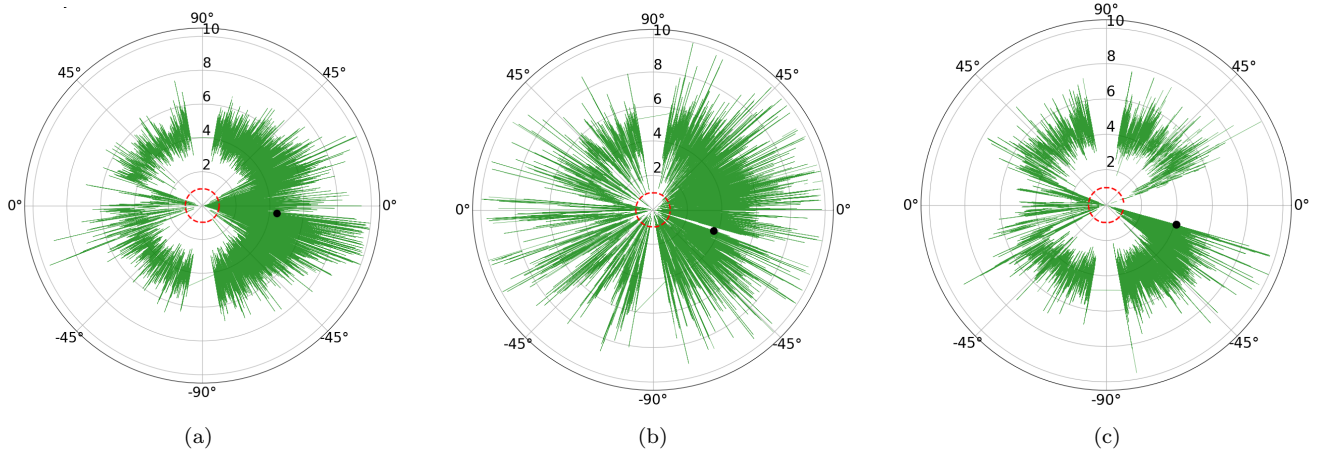


Figure 7. Helium abundance variation with heliographic latitudes. The dashed red circle shows $A_{He}=1\%$. The black dot shows the start time and the orbit progress clockwise. The Ulysses first (1992-1998), second (1999-2004) and third (2005-2009) orbit observations are shown. The first and third orbit shows low helium abundance events near the equatorial plane, whereas the 2nd orbit shows the events spread over all the heliographic latitudes.

near the HCS. Interestingly, our work based on 28 events from *Wind* and 4 from PSP reveal low A_{He} events near the heliospheric current sheet. In addition, almost all *Wind* events characteristically show low alpha density, slow speed, negligible alpha and proton speed difference, and similar temperatures. Therefore, we infer that all the events originated from similar sources in the corona. The source backtracing using the WSA model supports this inference. PSP observations also show similar properties. Similar observations are also reported in [Suess et al. \(2009\)](#). In their work, [Suess et al. \(2009\)](#) suggested that three potential locations associated with streamers can produce low helium abundance. These locations are the coronal hole, the streamer core just below the magnetic cusp, and the streamer legs (see, Figure 11 of [Suess et al. 2009](#)). The plasma from these three sources can be supplied in the following manner. First, there is a probability that the plasma from the coronal holes adjacent to streamers can enter the streamer region via Kelvin-Helmholtz (KH) instability ([Suess et al. 2009](#)). Second, the streamer core region, which is located just below the cusp, can contribute plasma via reconnection with open field lines. Third, the streamer legs can provide plasma to the streamers through open magnetic field lines. This description is consistent with three-fluid models of the slow solar wind in corona streamers that find gravitational settling of helium (as well as other heavy ions) in the core of streamers reducing their relative abundance in the streamer stalk, and outflow of these heavy ions at the streamer legs, due to the Coulomb friction with slow solar wind stream electrons and protons ([Ofman 2004a](#); [Ofman & Kramar 2010](#); [Abbo et al. 2016](#)).

To understand the contribution of coronal hole plasma, we compared the Fe/O vs A_{He} density distribution for fast and slow solar wind events using ACE satellite data from 1998 to 2020 (Figure 5). It can be seen from Figure 5 that these events significantly deviate from the distribution of fast wind, suggesting a minimal contribution from coronal hole plasma. These events show higher Fe/O ratio, indicating substantial influence of the FIP effect. This also suggests that the plasma comes from longer loops, resulting in a higher FIP processing ([Laming 2015](#)). However, as suggested by [Laming et al. \(2019\)](#), the FIP effect alone cannot explain the low helium abundances; therefore, we explore other possibilities as well.

The next possibility is that the low A_{He} plasma comes from the streamers' cores or the streamer's legs. [Suess et al. \(2009\)](#) also showed a good correlation between O/H and He/H and argued that O/H is reduced in the core of the streamers compared to the legs. Therefore, they suggested that streamer cores could be potential sources of low A_{He} winds. The low A_{He} events were proposed as transient events. Further, depleted helium abundance is mostly observed towards one edge of the HCS. The streamer core region located just below the cusp can release plasma from a specific side, leading to a depletion of A_{He} on that side of the HCS.

[Suess et al. \(2009\)](#) suggested that plasma blobs are released through the cusp of the streamers. The sharply pinched magnetic field confines the plasma, and this plasma can be released easily by small pressure pulses. These small perturbations cause an episodic release of low A_{He} plasma. The streamer cusp, probably pinching off by reconnection and destabilized by Alfvén waves, can release the plasma with low A_{He} . The resonant period for such waves (i.e., the

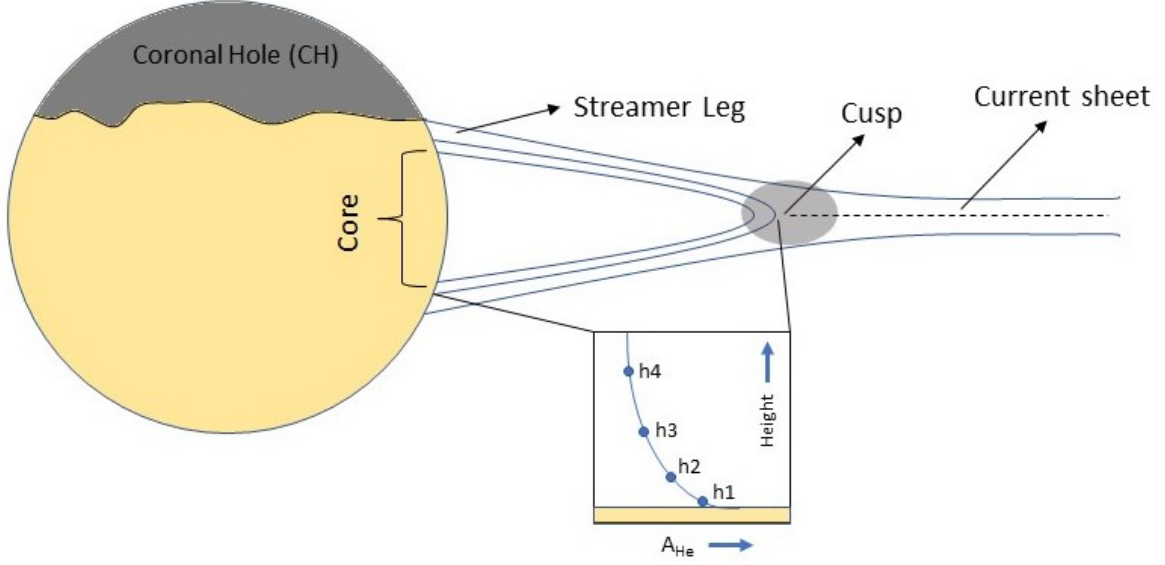


Figure 8. The schematic structure of the streamers. The (ideal) gravitationally settled helium abundance profile is shown. The reduction in helium abundance in the solar wind is attributed to the release of plasma from higher altitudes, e.g., the solar wind coming from h4 will have less A_{He} as compared to wind from h1. The zoomed version is rotated by 90° .

travel time from one footpoint to the other) is on the order of 10^3 seconds (Gershkovich et al. (2023)), coronal loop length/Alfvén speed $\sim 10^{11}$ cm/ 10^8 cm/s). This period is evident in solar wind signatures and can be seen in Figure 6 and in supplementary Table S3.

Another important point is that the quiescent streamer cores are the only structures stable and quiescent enough to allow gravitational settling, which can lead to a very low A_{He} as well as of other heavy ions in the solar wind as demonstrated by the three-fluid models (e.g., Ofman 2004a; Ofman & Kramar 2010; Ofman et al. 2015; Abbo et al. 2019). Figure 8 shows three potential sources of solar wind similar to Suess et al. (2009). The three sources are the streamer leg, coronal hole, and cusp. The core of the streamer can be regarded as the ideal location for gravitational settling to occur. The (ideal) profile of gravitationally settled helium abundance is shown in the square box, which is rotated by 90° . Following this in Figure 8, if we consider gravitational stratification in the streamers, the solar wind coming from height h4 will have lower A_{He} as compared to wind from height h1. So, the solar wind released from the streamer cusps can show a very low helium abundance. Note, in the above discussion, the interplanetary modulation causing the changes in A_{He} (Yogesh et al. 2023) is ignored because the low A_{He} events are observed by PSP near the Sun as well as at 1 AU by *Wind*.

The low A_{He} events are also observed by Ulysses. The A_{He} variation during three different Ulysses orbits (Figure 7) represent different phases of the solar cycle. These distributions are similar to the distribution of the streamers during the solar maxima and minima (Owens et al. 2014). During solar minimum, there are longer duration events with lower A_{He} values compared to solar maximum (not shown in the paper). This intriguing feature can be attributed to the lifetime variability of streamers during the solar cycle (Owens et al. 2014). During solar maximum, the streamers are distributed towards the higher heliolatitudes and are short-lived compared to the long and stable streamers during solar minima. Furthermore, the dominant presence of solar wind originating from streamers typically exhibits lower A_{He} values. So, the Ulysses observations also suggest that the low A_{He} events originate from streamers. This variation of A_{He} in streamers can also explain the solar cycle variation in A_{He} , as suggested by Kasper et al. (2007), where they proposed that the dominance of streamers as the source of A_{He} during solar minima could result in lower A_{He} values compared to solar maxima.

Finally, observing low A_{He} events in the extended solar wind requires specific conditions. The present investigation explains the sources of these low A_{He} events. However, to understand the quantitative aspects, detailed modeling of the streamer cusp regions and the altitudes from which the solar wind originates is still required. This aspect is beyond the scope of this paper.

5. CONCLUSIONS

The very low helium abundance events ($A_{He} < 1\%$) are a unique feature of the slow solar wind and are observed throughout the heliosphere. These events are generally characterized by very low solar wind speed and negligible differential streaming between the alphas and protons in the case of *Wind* events. In contrast, events observed by PSP show speed that is smaller compared to other times but not negligible. The ADAPT-WSA model analysis indicates that these low A_{He} solar wind parcels originate from quiet Sun coronal helmet streamers. This was also supported using the Ulysses observations. The Ulysses observations showed that these events are distributed along the heliolatitude during the solar maxima, whereas they are distributed near the equator during the solar minima. These distributions are similar to how streamers are distributed during the solar maxima and minima (Owens et al. 2014). In other words, these Ulysses observations are also consistent with the inference that low A_{He} events originate in quiet Sun coronal hole streamers.

It has been proposed in the past that coronal streamers can release plasma through interaction with coronal hole boundaries, streamer legs and streamer core. Here, it has been demonstrated using compositional proxies that the coronal hole plasma is not released from streamer legs. Instead, the streamer cusps situated above the core of the streamer act as a source region. Based on the frequencies observed in A_{He} , this release of low A_{He} parcels from the streamer cusps are likely triggered by Alfvén waves. The sharply pinched magnetic field confines the plasma, and this plasma can be released easily through magnetic reconnection triggered by small perturbations caused by Alfvén waves. The signatures of these waves are also observed in these events. The streamer cores are the only structures stable and quiescent enough to allow gravitational settling, which can lead to a very low A_{He} in the solar wind. This low A_{He} plasma is released from the tops of streamers. The reported low helium abundance is consistent with multi-fluid models of streamers, demonstrating the gravitational settling of helium ions in quiescent streamer cores and associated depletion of helium in the slow solar wind.

6. ACKNOWLEDGEMENT

We thank Prof. J. Martin Laming and Dr. Samantha Wallace for their constructive input and suggestions for this work. We also thank the WSA model development team at NASA/GSFC for providing model runs for our event list. We thank the PIs of ACE, *Wind* and Ulysses spacecraft. Parker Solar Probe was designed, built, and is now operated by the Johns Hopkins Applied Physics Laboratory as part of NASA's Living with a Star (LWS) program (contract NNN06AA01C). Support from the LWS management and technical team has played a critical role in the success of the Parker Solar Probe mission. We thank NASA/GSFC for providing the facilities to carry out this work. Yogesh also thank SCOSTEP for the opportunity as a Visiting Scholar, under which this work was accomplished. This work is supported by the Department of Space, Government of India. Yogesh and L.O. acknowledge support by NSF grant AGS-2300961, L.O. acknowledges support by NASA LWS grant 80NSSC20K0648. NG is supported by NASA's LWS program and the STEREO project. PM acknowledges the support from NASA HGIO grant 80NSSC23K0419.

REFERENCES

- Abbo, L., Giordano, S., & Ofman, L. 2019, *A&A*, 623, A95, doi: [10.1051/0004-6361/201834299](https://doi.org/10.1051/0004-6361/201834299)
- Abbo, L., Ofman, L., Antiochos, S. K., et al. 2016, *SSRv*, 201, 55, doi: [10.1007/s11214-016-0264-1](https://doi.org/10.1007/s11214-016-0264-1)
- Alterman, B. L., & Kasper, J. C. 2019, *ApJL*, 879, L6, doi: [10.3847/2041-8213/ab2391](https://doi.org/10.3847/2041-8213/ab2391)
- Alterman, B. L., Kasper, J. C., Leamon, R. J., & McIntosh, S. W. 2021, *SoPh*, 296, 67, doi: [10.1007/s11207-021-01801-9](https://doi.org/10.1007/s11207-021-01801-9)
- Alterman, B. L., Kasper, J. C., Stevens, M. L., & Koval, A. 2018, *ApJ*, 864, 112, doi: [10.3847/1538-4357/aad23f](https://doi.org/10.3847/1538-4357/aad23f)
- Altschuler, M. D., & Newkirk, G. 1969, *SoPh*, 9, 131, doi: [10.1007/BF00145734](https://doi.org/10.1007/BF00145734)
- Arge, C. N., Henney, C., Koller, J., et al. 2009, in *AGU Fall Meeting Abstracts*, Vol. 2009, SM54A-06
- Arge, C. N., Henney, C. J., Hernandez, I. G., et al. 2013, in *American Institute of Physics Conference Series*, Vol. 1539, *Solar Wind 13*, ed. G. P. Zank, J. Borovsky, R. Bruno, J. Cirtain, S. Cranmer, H. Elliott, J. Giacalone, W. Gonzalez, G. Li, E. Marsch, E. Moebius, N. Pogorelov, J. Spann, & O. Verkhoglyadova, 11–14, doi: [10.1063/1.4810977](https://doi.org/10.1063/1.4810977)

- Arge, C. N., Henney, C. J., Koller, J., et al. 2010, in American Institute of Physics Conference Series, Vol. 1216, Twelfth International Solar Wind Conference, ed. M. Maksimovic, K. Issautier, N. Meyer-Vernet, M. Moncuquet, & F. Pantellini, 343–346, doi: [10.1063/1.3395870](https://doi.org/10.1063/1.3395870)
- Arge, C. N., Luhmann, J. G., Odstrcil, D., Schrijver, C. J., & Li, Y. 2004, *Journal of Atmospheric and Solar-Terrestrial Physics*, 66, 1295, doi: [10.1016/j.jastp.2004.03.018](https://doi.org/10.1016/j.jastp.2004.03.018)
- Arge, C. N., Odstrcil, D., Pizzo, V. J., & Mayer, L. R. 2003a, in American Institute of Physics Conference Series, Vol. 679, *Solar Wind Ten*, ed. M. Velli, R. Bruno, F. Malara, & B. Bucci, 190–193, doi: [10.1063/1.1618574](https://doi.org/10.1063/1.1618574)
- Arge, C. N., Odstrcil, D., Pizzo, V. J., & Mayer, L. R. 2003b, in *Solar Wind Ten*, ed. M. Velli, R. Bruno, F. Malara, & B. Bucci, Vol. CS-679, Am. Inst. Phys., Melville, 190–193, doi: [10.1063/1.1618574](https://doi.org/10.1063/1.1618574)
- Arge, C. N., & Pizzo, V. J. 2000, *J. Geophys. Res.*, 105, 10465, doi: [10.1029/1999JA000262](https://doi.org/10.1029/1999JA000262)
- Bale, S. D., Goetz, K., Harvey, P. R., et al. 2016, *SSRv*, 204, 49, doi: [10.1007/s11214-016-0244-5](https://doi.org/10.1007/s11214-016-0244-5)
- Bame, S. J., McComas, D. J., Barraclough, B. L., et al. 1992, *A&AS*, 92, 237
- Borrini, G., Gosling, J. T., Bame, S. J., Feldman, W. C., & Wilcox, J. M. 1981, *J. Geophys. Res.*, 86, 4565, doi: [10.1029/JA086iA06p04565](https://doi.org/10.1029/JA086iA06p04565)
- Fu, H., Madjarska, M. S., Li, B., Xia, L., & Huang, Z. 2018, *MNRAS*, 478, 1884, doi: [10.1093/mnras/sty1211](https://doi.org/10.1093/mnras/sty1211)
- Gershkovich, I., Lepri, S., Viall, N., Di Matteo, S., & Kepko, L. 2023, *SoPh*, 298, 89, doi: [10.1007/s11207-023-02176-9](https://doi.org/10.1007/s11207-023-02176-9)
- Giordano, S., Fineschi, S., Ofman, L., Mancuso, S., & Abbo, L. 2007, in *ESA Special Publication*, Vol. 641, *Second Solar Orbiter Workshop*, ed. E. Marsch, K. Tsinganos, R. Marsden, & L. Conroy, 31
- Gloeckler, G., Cain, J., Ipavich, F. M., et al. 1998, *SSRv*, 86, 497, doi: [10.1023/A:1005036131689](https://doi.org/10.1023/A:1005036131689)
- Hickmann, K. S., Godinez, H. C., Henney, C. J., & Arge, C. N. 2015, *SoPh*, 290, 1105, doi: [10.1007/s11207-015-0666-3](https://doi.org/10.1007/s11207-015-0666-3)
- Higginson, A. K., Antiochos, S. K., DeVore, C. R., Wyper, P. F., & Zurbuchen, T. H. 2017, *ApJ*, 837, 113, doi: [10.3847/1538-4357/837/2/113](https://doi.org/10.3847/1538-4357/837/2/113)
- Hoeksema, J. T., Wilcox, J. M., & Scherrer, P. H. 1983, *J. Geophys. Res.*, 88, 9910, doi: [10.1029/JA088iA12p09910](https://doi.org/10.1029/JA088iA12p09910)
- Kasper, J. C., Stevens, M. L., Lazarus, A. J., Steinberg, J. T., & Ogilvie, K. W. 2007, *ApJ*, 660, 901, doi: [10.1086/510842](https://doi.org/10.1086/510842)
- Kasper, J. C., Abiad, R., Austin, G., et al. 2016, *SSRv*, 204, 131, doi: [10.1007/s11214-015-0206-3](https://doi.org/10.1007/s11214-015-0206-3)
- Kasper, J. C., Klein, K. G., Weber, T., et al. 2017, *ApJ*, 849, 126, doi: [10.3847/1538-4357/aa84b1](https://doi.org/10.3847/1538-4357/aa84b1)
- Kepko, L., Viall, N. M., & DiMatteo, S. 2024, *Journal of Geophysical Research (Space Physics)*, 129, e2023JA031403, doi: [10.1029/2023JA031403](https://doi.org/10.1029/2023JA031403)
- Laming, J. M. 2015, *Living Reviews in Solar Physics*, 12, 2, doi: [10.1007/lrsp-2015-2](https://doi.org/10.1007/lrsp-2015-2)
- Laming, J. M., Vourlidas, A., Korendyke, C., et al. 2019, *ApJ*, 879, 124, doi: [10.3847/1538-4357/ab23f1](https://doi.org/10.3847/1538-4357/ab23f1)
- Lepping, R. P., Acuña, M. H., Burlaga, L. F., et al. 1995, *SSRv*, 71, 207, doi: [10.1007/BF00751330](https://doi.org/10.1007/BF00751330)
- Livi, R., Larson, D. E., Kasper, J. C., et al. 2022, *ApJ*, 938, 138, doi: [10.3847/1538-4357/ac93f5](https://doi.org/10.3847/1538-4357/ac93f5)
- Lynch, B. J., Edmondson, J. K., & Li, Y. 2014, *SoPh*, 289, 3043, doi: [10.1007/s11207-014-0506-x](https://doi.org/10.1007/s11207-014-0506-x)
- McGregor, S. L., Hughes, W. J., Arge, C. N., & Owens, M. J. 2008, *Journal of Geophysical Research: Space Physics*, 113, doi: <https://doi.org/10.1029/2007JA012330>
- Moses, J. D., Antonucci, E., Newmark, J., et al. 2020, *Nature Astronomy*, 4, 1134, doi: [10.1038/s41550-020-1156-6](https://doi.org/10.1038/s41550-020-1156-6)
- Mostafavi, P., Allen, R. C., McManus, M. D., et al. 2022, *ApJL*, 926, L38, doi: [10.3847/2041-8213/ac51e1](https://doi.org/10.3847/2041-8213/ac51e1)
- Mostafavi, P., Allen, R. C., Jagarlamudi, V. K., et al. 2024, *A&A*, 682, A152, doi: [10.1051/0004-6361/202347134](https://doi.org/10.1051/0004-6361/202347134)
- Ofman, L. 2004a, *Advances in Space Research*, 33, 681, doi: [10.1016/S0273-1177\(03\)00235-7](https://doi.org/10.1016/S0273-1177(03)00235-7)
- . 2004b, *Journal of Geophysical Research (Space Physics)*, 109, A07102, doi: [10.1029/2003JA010221](https://doi.org/10.1029/2003JA010221)
- Ofman, L., & Kramar, M. 2010, in *Astronomical Society of the Pacific Conference Series*, Vol. 428, *SOHO-23: Understanding a Peculiar Solar Minimum*, ed. S. R. Cranmer, J. T. Hoeksema, & J. L. Kohl, 321, doi: [10.48550/arXiv.1004.4847](https://doi.org/10.48550/arXiv.1004.4847)
- Ofman, L., Provornikova, E., Abbo, L., & Giordano, S. 2015, *Annales Geophysicae*, 33, 47, doi: [10.5194/angeo-33-47-2015](https://doi.org/10.5194/angeo-33-47-2015)
- Ofman, L., Yogesh, & Giordano, S. 2024, *The Astrophysical Journal Letters*, 970, L16, doi: [10.3847/2041-8213/ad5e7e](https://doi.org/10.3847/2041-8213/ad5e7e)
- Ofman, L., Boardsen, S. A., Jian, L. K., et al. 2023, *ApJ*, 954, 109, doi: [10.3847/1538-4357/acea7e](https://doi.org/10.3847/1538-4357/acea7e)
- Ogilvie, K. W., Chornay, D. J., Fritzenreiter, R. J., et al. 1995, *SSRv*, 71, 55, doi: [10.1007/BF00751326](https://doi.org/10.1007/BF00751326)
- Owens, M. J., Crooker, N. U., & Lockwood, M. 2014, *Journal of Geophysical Research (Space Physics)*, 119, 36, doi: [10.1002/2013JA019412](https://doi.org/10.1002/2013JA019412)
- Riley, P., Linker, J. A., & Arge, C. N. 2015, *Space Weather*, 13, 154, doi: [10.1002/2014SW001144](https://doi.org/10.1002/2014SW001144)

- Riley, P., Linker, J. A., & Mikić, Z. 2001, *J. Geophys. Res.*, 106, 15889, doi: [10.1029/2000JA000121](https://doi.org/10.1029/2000JA000121)
- Sanchez-Diaz, E., Rouillard, A. P., Lavraud, B., et al. 2016, *Journal of Geophysical Research (Space Physics)*, 121, 2830, doi: [10.1002/2016JA022433](https://doi.org/10.1002/2016JA022433)
- Schatten, K. H. 1971, *Cosmic Electrodynamics*, 2, 232
- Schatten, K. H., Wilcox, J. M., & Ness, N. F. 1969, *SoPh*, 6, 442, doi: [10.1007/BF00146478](https://doi.org/10.1007/BF00146478)
- Schwadron, N. A., McComas, D. J., Elliott, H. A., et al. 2005, *Journal of Geophysical Research (Space Physics)*, 110, A04104, doi: [10.1029/2004JA010896](https://doi.org/10.1029/2004JA010896)
- Stone, E. C., Frandsen, A. M., Mewaldt, R. A., et al. 1998, *SSRv*, 86, 1, doi: [10.1023/A:1005082526237](https://doi.org/10.1023/A:1005082526237)
- Suess, S. T., Ko, Y. K., von Steiger, R., & Moore, R. L. 2009, *Journal of Geophysical Research (Space Physics)*, 114, A04103, doi: [10.1029/2008JA013704](https://doi.org/10.1029/2008JA013704)
- Vasquez, B. J., Farrugia, C. J., Simunac, K. D. C., Galvin, A. B., & Berdichevsky, D. B. 2017, *Journal of Geophysical Research (Space Physics)*, 122, 1487, doi: [10.1002/2016JA023636](https://doi.org/10.1002/2016JA023636)
- Đurovcová, T., Němeček, Z., & Šafránková, J. 2019, *ApJ*, 873, 24, doi: [10.3847/1538-4357/ab01c8](https://doi.org/10.3847/1538-4357/ab01c8)
- Wallace, S., Arge, C. N., Viall, N., & Pihlström, Y. 2020, *ApJ*, 898, 78, doi: [10.3847/1538-4357/ab98a0](https://doi.org/10.3847/1538-4357/ab98a0)
- Wang, Y. M., & Sheeley, N. R., J. 1990, *ApJ*, 355, 726, doi: [10.1086/168805](https://doi.org/10.1086/168805)
- . 1992, *ApJ*, 392, 310, doi: [10.1086/171430](https://doi.org/10.1086/171430)
- Wang, Y. M., Sheeley, N. R., Socker, D. G., Howard, R. A., & Rich, N. B. 2000, *J. Geophys. Res.*, 105, 25133, doi: [10.1029/2000JA000149](https://doi.org/10.1029/2000JA000149)
- Woolley, T., Matteini, L., McManus, M. D., et al. 2021, *MNRAS*, 508, 236, doi: [10.1093/mnras/stab2281](https://doi.org/10.1093/mnras/stab2281)
- Worden, J., & Harvey, J. 2000, *SoPh*, 195, 247, doi: [10.1023/A:1005272502885](https://doi.org/10.1023/A:1005272502885)
- Yogesh, Chakrabarty, D., & Srivastava, N. 2021, *MNRAS*, 503, L17, doi: [10.1093/mnrasl/slab016](https://doi.org/10.1093/mnrasl/slab016)
- . 2022, *MNRAS*, 513, L106, doi: [10.1093/mnrasl/slac044](https://doi.org/10.1093/mnrasl/slac044)
- . 2023, *MNRAS*, 526, L13, doi: [10.1093/mnrasl/slad112](https://doi.org/10.1093/mnrasl/slad112)